Chapter 8

Fischer-Tropsch Synthesis Investigation in a Gas-Inducing Agitated Reactor Using Electrical Capacitance Tomography

Bawadi Abdullah, Chirag Dave, Cyrus G. Cooper, Tuan Huy Nguyen, and Adesoji A. Adesina*

**Reactor Engineering & Technology Group,
School of Chemical Engineering,
The University of New South Wales,
Sydney, New South Wales, Australia 2052
*E-mail: a.adesina@unsw.edu.au**

Non-intrusive electrical capacitance tomography (ECT) has been used to analyse the dynamic feedback between the fluid phase characteristics (such as dispersed phase hold-up, mixing time constants, etc) and reaction metrics in gas-liquid-solid reactor using the Fischer-Trospch synthesis (FTS) as a case study. The coupling between these two processes (transport and reaction) is due to the changing physicochemical properties of the liquid phase medium as product accumulates with reaction progression. Gas recirculation within the reactor was improved by using a gas-inducing impeller at speeds above the minimum required for gas entrainment (293 rpm) thus ensuring better gas conversion per pass. The steady-state gas phase hold-up, ε_G, dependency on temperature was due to contributions from both thermal expansion and reaction-induced changes in the liquid phase. The behaviour was adequately captured by the 3-parameter Chapman-Richards model, which combined with the Arrhenius representation of the rate behaviour to yield a new relation that coupled the dispersed phase hold-up and reaction rate. The advantages of using this model for inferential control or optimization purposes is immediately evident. Several runs conducted in the range 473-533 K at different operating pressures (1, 11 and 21 atm) and wide spectrum of feed H_2:CO

ratio (1:5 to 5:1) over a 36-hour period permitted further development of ECT-based models for chain growth factor, olefin-to-paraffin ratio and the thermotemporal relationship for dispersed phase hold-up in an FT slurry reactor. The effect of total operating pressure was relatively modest compared to temperature on both FT reaction metrics and dispersed phase hold-up.

Introduction

The slurry reactor is particularly suitable for hydrocarbon synthesis from CO hydrogenation over Fe and Co catalysts because of its ability to achieve better control of the exothermic reaction and better catalyst usage (*1*, *2*). However, the complex hydrodynamics involved and the impact of changing liquid physicochemical properties as a result of products dissolution in the liquid phase have led to compounded reactor analysis and scale-up challenges (*3*). Possible variation in dispersed phase hold-up and spatial distribution may give rise to unexpected results even in the absence of mass transport resistances. Within the last two decades, several investigators, including Joshi and co-workers (*4–6*), have reported the advantages of the gas-inducing stirred tank (GIST) in the provision of improved mixing and single gas conversion per pass over conventional agitators. The associated hydrodynamics, mixing and mass transfer characteristics have been examined using residence-time distribution (RTD) and computational fluid dynamics methods to secure correlations for design and scale-up purposes. The increased gas recirculation also promotes solid mixing and hence better catalyst utilization when applied in a slurry reactor. However, the agitation rate msut exceed the critical impeller speed, N_{sc}, given by the Sawant-Joshi criterion (*7*) for the gas-inducing stirrer before the benefits of enhanced gas recirculation may be realized. For a slurry reactor, N_{sc}, is well below the rotational speed necessary to ensure absence of gas absorption and external liquid-solid transport resistances.

In view of the product-induced changes in the fluid phase properties in a multiphase reactor – e.g. viscosity, density and surface tension - and hence, phase holdup variation with time-on-stream during reaction, a non-invasive evaluation of the reactor would provide useful insight into the coupling effect of transport processes and reaction metrics. Indeed, non-intrusive flow visualization of the reactor contents with time-on-stream may provide additional information to complement standard chromatographic exit gas phase composition analysis leading to better understanding and ability to carry out superior scale-up and modeling, for example, using computational fluid dynamics approach (*8*). This is especially germane to FT operation in a mechanically-agitated slurry reactor fitted with a gas-entrainment impeller to improve gas recirculation and hence, CO conversion per pass. In this paper, we report the first investigation of in-situ electrical capacitance tomography diagnosis of the Fischer-Tropsch reaction. The objective was to determine the relationship between reaction metrics and dispersed phase hold-up characteristics with time-on-stream.

Materials and Method

Catalyst Preparation and Characterisation

The catalyst ($10wt\%Co/Al_2O_3$) was synthesised by impregnating requisite amount of cobalt nitrate solution onto spray-dried gamma-alumina particles (60-90 μm obtained from Saint-Gobain Nopro Corporation, USA) at 298 K for 3 h under constant stirring and pH of 3.6 (5M HNO_3 solution as pH control) using a Metler-Toledo T90 Titration Excellence system. The resulting slurry was dried in the oven at 303 K for 20 h. The dried catalyst was then calcined in an oven at 673 K for 5 h at rate of 5 K min^{-1}. The calcined catalyst was further crushed and sieved to 45-90 μm using Retsch AS 200 Analytical Sieve Shaker and loaded into stainless steel fixed bed reactor (OD = 12.5 mm) where it was activated at 623 K for 8 h in 5% CO/H_2 mixture at a heating rate of 5 K min^{-1}. High purity research grade H_2 (99.99%), CO(99.99%) and N_2(99.99%) supplied by Linde (Sydney) were used in all runs. Gas flowrates were controlled and metered via calibrated mass flow controllers (Brooks 5850E).

BET surface area and pore volume were obtained from N_2 physisorption measurements at 77 K on a Quantachrome Autosorb-1 unit while acid-base properties were determined via NH_3 and CO_2-TPD respectively on Micromeritics Autochem 2910 using 5 heating rates (5-30 K min^{-1}) for up to 973 K. H_2 chemisorption on the same unit provided the metal dispersion and crystallite size. X-ray diffractograms from Philips X'pert MPD (at 45 kV, 40 mA and 0.2°min^{-1}(2θ)) were used to identify the solid oxide phases present in the catalyst.

Reactor Characterisation and ECT Set-Up

The experimental system depicted in Figure 1 consists of a gas manifold-station, an electrical capaictiance tomography (ECT) module connected to the 2-litre Parr stainless steel reactor (ID = 105 mm) via a 12-electrode cylindrical basket sensor snuggly fitted around the perimeter of the vessel. The stainless steel electrode has a temperature-resistant coating to permit operation up to 553 K and pressure to 30 atm.

The reactor was mounted in a temperature-controlled electrical furnace and equipped with a gas-inducing stirrer as illustrated in Figure 2. The gas-inducing mixer comprises of hollow shaft with gas inlet port at the top (125 mm above the liquid surface) and a 4-blade flat impeller - each blade has 3 gas outlet ports -with a clearance of 60 mm from the reactor base. The final section is a product collection and analysis station consisting of two condensers placed downstream of the reactor (for C_{7+} hydrocarbons and water removal) and a Shimadzu gas chromatograph (model GC17A) for product composition determination. The activated catalyst is transferred under a N_2 blanket pneumatically into the reactor containing paraffin oil (boiling point 633 K) maintained at the reaction temperature prior to the FT runs.
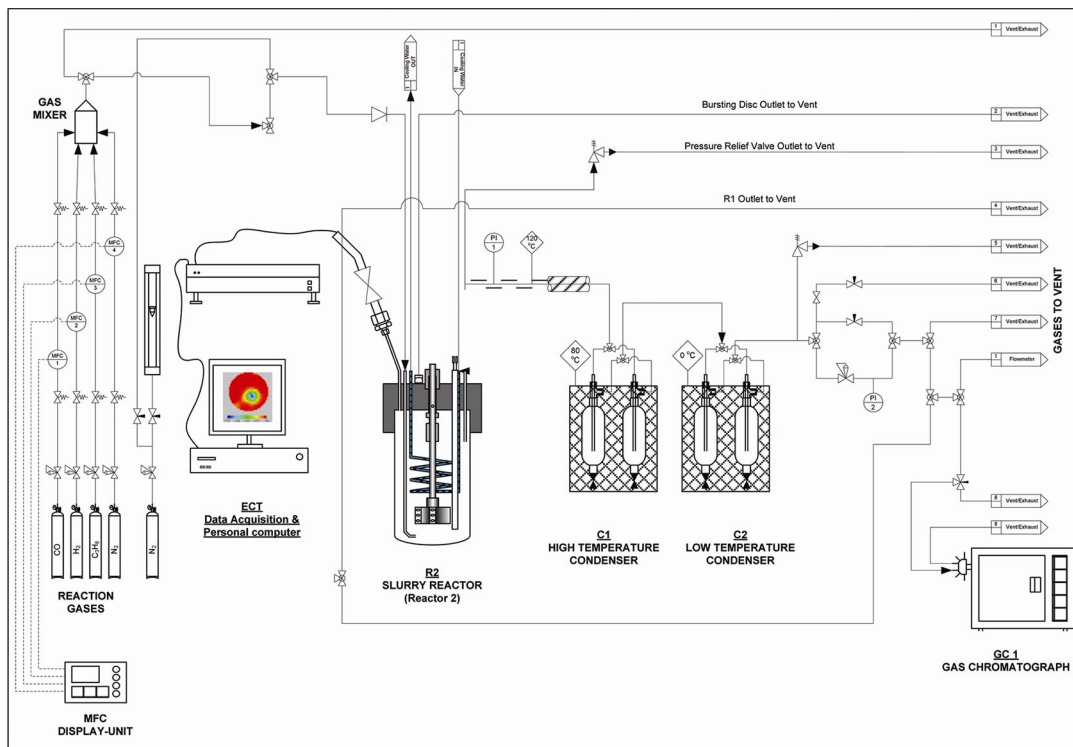
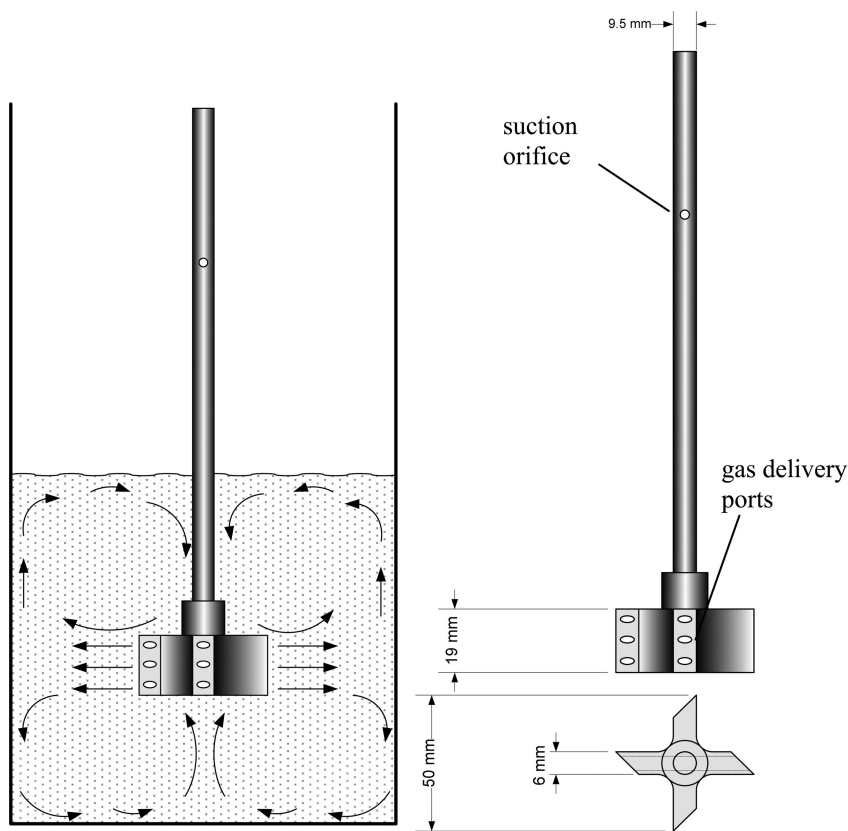*Figure 1. Experimental apparatus for the Fischer-Tropsch synthesis study.*

Figure 2. Schematic of the gas-inducing impeller.

The minimum stirring speed required for gas induction through the gas inlet port on the shaft was estimated from the Sawant-Joshi equation (7) given by:

$$\frac{N_{sc}^2 D_I^2}{gh}\left(\frac{\mu}{\mu_{water}}\right) = 0.21 \tag{1}$$

may be used to estimate the critical agitation speed, N_{sc}, where h is the impeller submersion depth, D_I = impeller diameter, μ is the liquid phase viscosity, μ_{water} is the water viscosity while g is the acceleration due to gravity. For the present stirred tank arrangement, h = 56 mm, D_I = 50 mm and the liquid phase was water, μ/μ_{water} =1.93 which gives N_{sc} = 4.9 rps (293 rpm). As a result preliminary investigation of the effect of stirring speed on reaction rate was done with agitation rate greater than 300 rpm. Indeed, to avoid both external mass transport and pore diffusional limitations, a stirring speed of 1200 rpm with catalyst average particle in the range 45-90 μm was used for all experiments.

The response of the experimental system to a step change in gas phase composition (from pure nitrogen to argon) under typical FTS temperature and pressure (cf. Figure 3) provided the transport lag and characteristic time constant for the fluid phase mixing. The ECT sensor was connected to a central processing module (M3000) – both supplied by Industrial Tomography Systems (ITS), Manchester, UK. Data analysis was carried out using the ITS M3000 Tool Suite. The software utilises a non-iterative algorithm based on linear back-projection for fast image reconstruction for real-time imaging of moving processes to provide relevant tomograms of the vessel radial cross-section at the sensor plane. Tomograms were recorded at 500 kHz over a 100-second interval at one frame per second to ensure excellent spatiotemporal resolution for each run. The reconstructed image during an experiment contained information about the cross-sectional distribution of electrical permittivity of the vessel contents within the measurement plane. Tomograms collected were analysed to obtain the cross-sectional average phase hold-up.
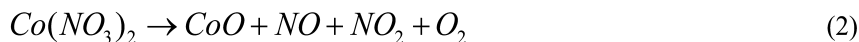
FT runs were carried out at total operating pressures between 1 to 21 atm and temperature, 473 to 533 K as well as H_2 feed composition, y_{H2} (0.0-1.0) The catalyst loading was kept constant at 10 gL^{-1} for all runs. The liquid products were collected in the hot and cold traps located downstream of the Parr reactor. The uncondensed gases passed through the back-pressure regulator for analysis on the Shimadzu GC (model 17A) using 30m GS-Q capillary column. A bubble flowmeter was used to measure the non-condensable gas flow rate prior to analysis. Although hydrocarbon formation rates were obtained from the transient gas phase composition analysis from the GC, the liquid products from the hot and cold traps contained cumulative composition over the run period and so could not be used for instantaneous formation rate estimation. Even so, GC analysis of the liquid aliquots revealed only modest hydrocarbon quantities (ca.14 mol% C_8-C_{10} in the cold trap and 30.6 mol% C_{10}-C_{16}) with non-detectable alcohols or acids. Heptane was.used as the solvent carrier for dissolving the liquid products in each condenser.

Results and Discussion

Physicochemical Attributes

Table 1 summarises the physicochemical properties of the catalyst. The BET surface area and pore volume of 170.8 m^2 g^{-1} and 0.474 ml g^{-1} respectively are lower than the corresponding values for the calcined alumina support probably due to pore blockage by the Co oxide crystallites (*9*).

The formation of cobalt oxides during cobalt nitrate decomposition in the calcination phase proceeded according to the reactions given by Eqs. (2) to (4) below.

$$Co(NO_3)_2 \rightarrow CoO + NO + NO_2 + O_2 \tag{2}$$

$$3CoO + \frac{1}{2}O_2 \rightarrow Co_3O_4 \tag{3}$$

$$CoO + Al_2O_3 \rightarrow CoAl_2O_4 \qquad (4)$$

Qualitative examination of the crystalline phases present in the calcined cobalt catalyst was performed by X-ray diffractogram (XRD) analysis and the result is illustrated in Figure 4. The presence of multiple Co_3O_4 peaks ($2\theta = 31.2°$ and $18.5°$) and a cobalt aluminate phase ($CoAl_2O_4$) at the major peak of $2\theta = 32°$ is evident. The peaks at $44°$ and $64°$ represent the CoO phase. This XRD analysis reconfirmed the postulated phases during calcination process (*10, 11*)

Table 1. Physicochemical properties of alumina support and cobalt catalyst

Parameters	γ-alumina support (calcined in air at 673 K)	Co/Al₂O₃
BET area (m².g⁻¹)	205.1	170.8
Pore volume (cm³ g⁻¹)	0.62	0.47
Average pore size, (nm)	12.0	11.1
Metal dispersion (%)	-	0.72
Metal surface area (m²g⁻¹)	-	0.48
Active particle size (nm)	-	139.0
$\Delta H_{d,NH3}$ (kJ mol⁻¹) Acid site concentration (μmol m⁻²)	61.75 - 1.20 -	47.52 (Peak I) 73.80 (Peak II) 0.79 (Peak I) 2.47 (Peak II)
$\Delta H_{d,CO2}$ (kJ mol⁻¹) Basic site concentration (μmol m⁻²)	32.57 (Peak I) 42.61 (Peak II) 0.41 0.59	54.23 (Peak 1) 45.69 (Peak II) 0.03 0.04

Based on Figure 3, the slurry reactor system seems to follow first order with time delay, t_d=6 minutes and mixing time constant, τ=26 minutes estimated from a fit of the data to Eq. (5) for both Ar and N₂.

$$y_p = y_p^{ss}\left(1 - \exp\left(-\frac{(t-t_d)}{\tau}\right)\right) \text{ for Ar}$$

and $\qquad\qquad\qquad\qquad\qquad\qquad\qquad\qquad$ **(5)**

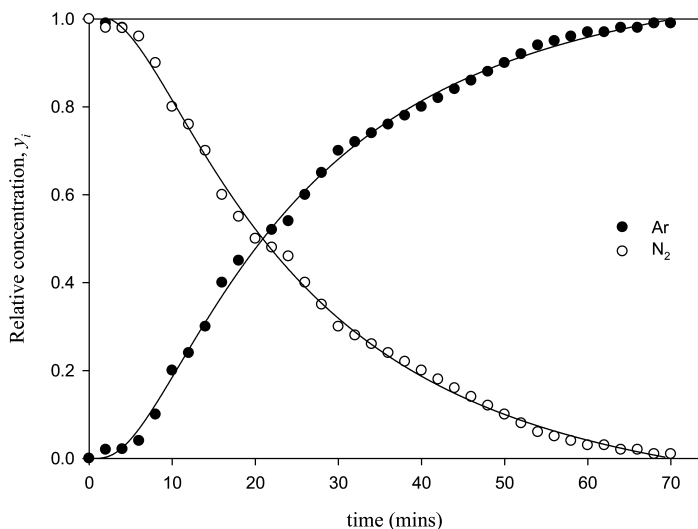$$y = y_0\left(1 - \exp\left(-\frac{(t-t_d)}{\tau}\right)\right) \text{ for N}_2$$

*Figure 3. Experimental system response to a step change in feed gas composition
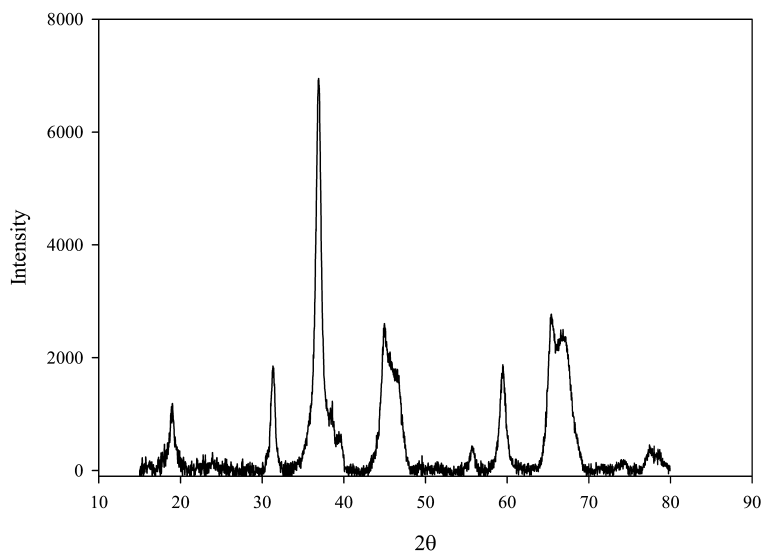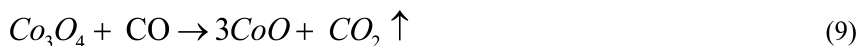(pure nitrogen to argon).*

Figure 4. XRD of a freshly calcined catalyst at 673 K.

In Synthetic Liquids Production and Refining; de Klerk, A., et al.;
ACS Symposium Series; American Chemical Society: Washington, DC, 2011.

The active sites for FTS were produced during the activation (reduction) stage (*12, 13*), namely;

$$Co_3O_4 + H_2 \rightarrow 3CoO + H_2O \uparrow \tag{6}$$

$$CoO + H_2 \rightarrow Co + H_2O \uparrow \tag{7}$$

$$CoAl_2O_4 + H_2 \rightarrow Co + Al_2O_3 + H_2O \uparrow \tag{8}$$

or

$$Co_3O_4 + CO \rightarrow 3CoO + CO_2 \uparrow \tag{9}$$

$$CoO + CO \rightarrow Co + CO_2 \uparrow \tag{10}$$

$$CoAl_2O_4 + CO \rightarrow Co + Al_2O_3 + CO_2 \uparrow \tag{11}$$

NH_3 temperature-desorption curves implicated the existence of two acid sites on the catalyst surface, namely; peak P1 located between 515-580 K and the second peak, P2 straddling 680-740 K. A fit of the data to,

$$\ln\left(\frac{\beta}{T_p^2}\right) = -\frac{\Delta H_d}{RT_p} + \frac{\Delta H_d A_{acid}}{RC} \tag{12}$$

gave straight lines in all cases having R-squared values of between 0.93 to 0.99 with slope and intercept used to evaluate the surface acidity parameters. Acid site strength and concentration on the solid sample are represented by the NH_3 heat of desorption, $(-\Delta H_d)$, and the acid site concentration, A_{acid}, respectively. The low temperature peak (P1) is a weak Lewis acid centre (*14*) while P2 appears to be a strong Lewis acid site since the corresponding NH_3 heat of desorption has a value of 73.8 kJ mol^{-1} (*15, 16*). Similar analysis performed on the pure alumina support calcined at 673 K revealed the presence of only the weak acid site (desorption peak at 529 to 568 K) although both weak and strong basic sites were present in the reduced catalyst. The strong Lewis acid centres may be due to the interaction between NH_3 and water formed during Co oxide reduction (which may be chemisorbed either on the Co site or metal-support interface) since the introduction of Co significantly increased this type of acid site concentration (from 1.2 μmol m^{-2} in calcined support and 3.17 μmol m^{-2} in the Co catalyst). However,, the weak basic sites seemed to decrease with addition of Ço species probably because they were supplanted by the strong acid sites during impregnation and and subsequent calcination.

Fischer-Trospch Reaction Metrics

ECT-Assisted Reactor Analysis

The dispersed phase hold-up, ε_D, was determined from the instantanenous tomograms (permittivity data) taken over the vessel cross-sectional area using the Maxwell equation (*17*) given as:

$$\varepsilon_D = \frac{2\chi_C + \chi_D - 2\chi_M - \chi_M\left(\dfrac{\chi_D}{\chi_C}\right)}{\chi_M - \left(\dfrac{\chi_D}{\chi_C}\right) + 2\left(\chi_C - \chi_D\right)} \tag{13}$$

where χ_C is the permittivity of the continuous phase (liquid), χ_D is the permittivity of dispersed phase (gas and catalyst particle) , and χ_M is the measured permittivity of the mixture obtained from pixel-averaged cross-sectional ECT data.

Figure 5 shows typical tomograms obtained from the reactor during a run. Since the ECT sensor cannot discriminate between a solid particle and the gas bubble, the dispersed phase hold-up, ε_D is a combination of the gas phase hold-up (ε_G) and the solid phase hold-up (ε_S).
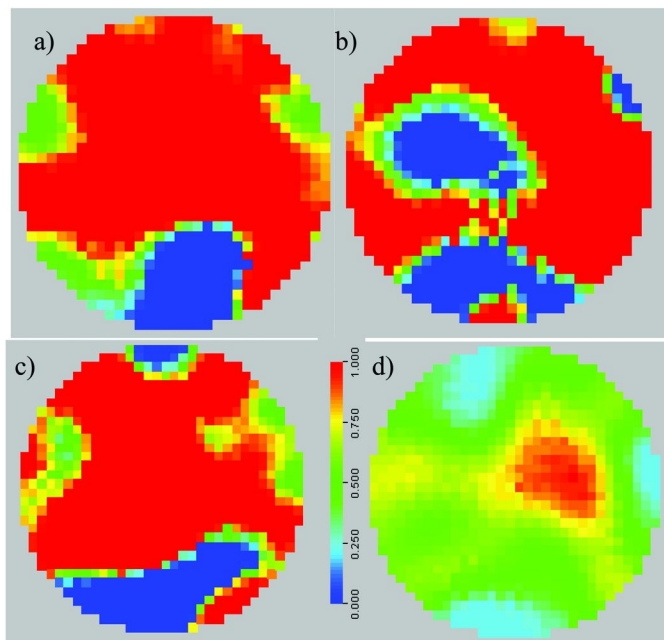

Figure 5. Tomography images at different temperature a)473 K b) 493 K c) 513 K and d) 533 K. The operating condition: Pressure: 21 atm, catalyst loading: 10g L⁻¹ stirring speed: 1200 rpm. (see color insert)

Preliminary experiments were carried using a conventional stirrer (with no gas inlet port on the shaft and exit ports on the impeller blades) with identical geometry and dimensions to the gas-inducing agitator (cf. Figure 2). Figure 6 reveals that the dispersed phase hold-up initially increased with solid loading for both impellers and seemed to level off at higher values.
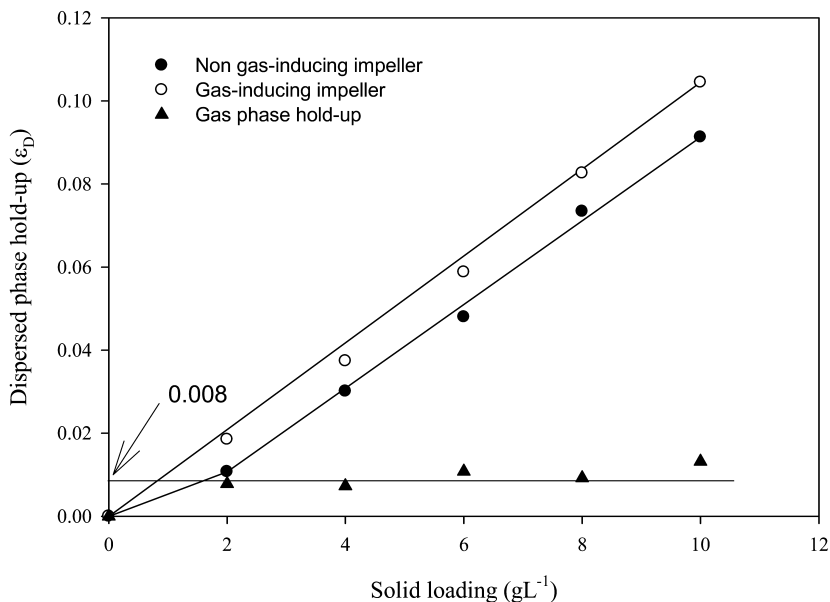

Figure 6. Dispersed holdup as function of solid loading for the two impellers used.

Both runs were conducted under non-reactive conditions with N_2 as the inert gas and alumina particles as the solid entities. Comparing the results for the conventional stirrer and gas-inducing stirrer shows that at the speed used (1200 rpm), there was a constant difference between the two stirrer types which represents the gas phase hold-up (since gas was not introduced into the reactor during the run with the conventional stirrer). Consequently, it may be assumed that the dispersed phase hold-up is simply the sum of the solid and gas phase hold-ups over the range of solid loading employed. Thus,

$$\varepsilon_D = \varepsilon_S + \varepsilon_G \tag{14}$$

Additionally, the effect of temperature on fluid phase permittivity (and hence, hold-up) was investigated.

As may be seen from Figure 7, the dispersed phase hold-up for the conventional stirrer was essentially invariant with temperature between 293-530 K (which covers the range for subsequent FTS runs).
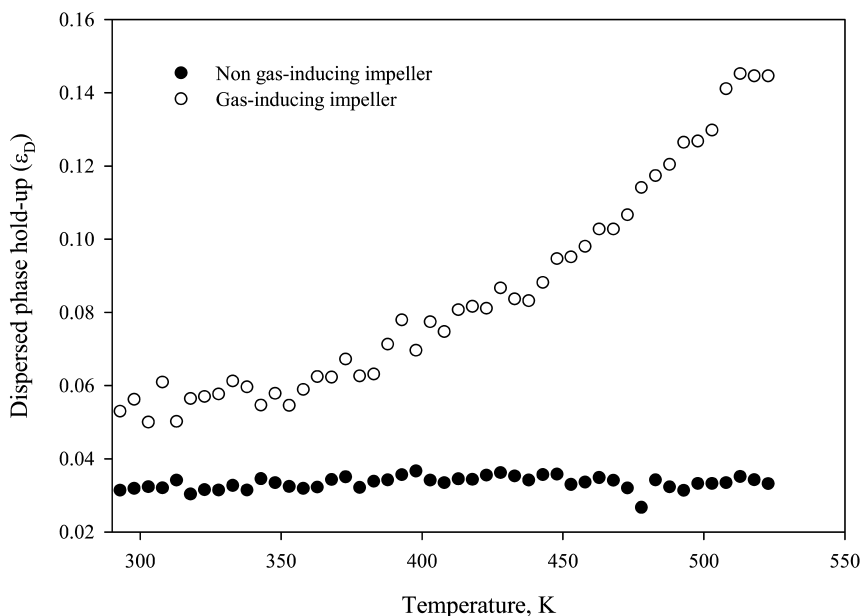
Figure 7. Effect of dispersed hold-up as function of temperature for different impeller geometry.

It would therefore seem that there was no significant change in the electrical permittivity of the alumina particles and the paraffin oil (used as the reaction medium) with temperature since the dispersed phase hold-up was constant. However, the data for the gas-inducing impeller demonstrated that the dispersed phase hold-up increased monotonically with temperature. The increased dispersed phase hold-up for the gas-inducing stirrer may be attributed to change only in the gas phase hold-up (consistent with the earlier results from Figure 6) which may be associated with volume increase due to gas expansion with increasing temperature. Given that the coefficient of expansion at constant pressure for a gas

is, $\frac{1}{V}\left(\frac{\partial V}{\partial T}\right)_P$, which is simply the reciprocal of the absolute temperature for an ideal gas, then the change witnessed in gas phase hold-up over the temperature

range used, may be given as, $\frac{V_2}{V_1} = \frac{T_2}{T_1} = \frac{\varepsilon_{G_2}}{\varepsilon_{G_1}}$) which is about 1.8 with T_1 and T_2 as 293 and 530 K respectively, in agreement with a doubling of the dispersed phase hold-up within the same temperature window in Figure 7. Indeed, a fit of the dispersed (gas) phase hold-up data for the gas-inducing impeller in Figure 7 to an Arrhenius expression yielded a low activation energy of 5.81 kJ mol^{-1} indicative of a purely physical process such as gas diffusion or solubility in liquids. As a result of these initial considerations, changes in dispersed phase

hold-up during isothermal FTS reaction may be readily decoupled from thermal expansion effects.

The influence of total operating pressure on the dispersed phase hold-up was also examined. Figure 8 evinces a linear, albeit gentle, increase in dispersed phase hold-up with increased operating pressure. The behaviour is readily captured by;

$$\varepsilon_D = \varepsilon_{D_0,P} + \lambda P \tag{15}$$

where, $\varepsilon_{D0,P}$ is the dispersed phase hold-up at atmospheric conditions, P is the total operating gauge pressure and λ an empirical constant for the syngas in paraffin oil. Linear regression gave ε_{G0} and λ as 0.112 and 5×10^{-4} atm^{-1} respectively.

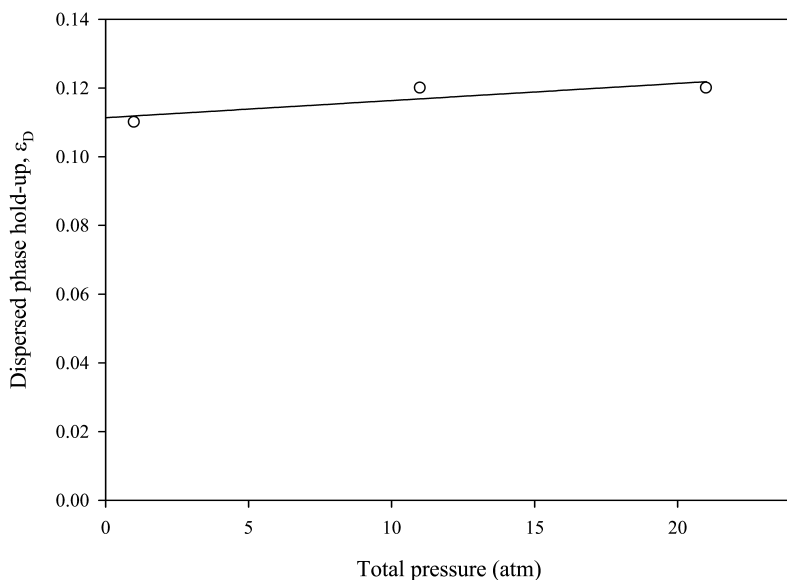*Figure 8. Dispersed phase hold-up as function of total pressure for reaction conditions:T = 498 K, and syngas with H$_2$:CO ratio = 2:1.*

Cooper *et al.* (*13*) had previously shown that external transport and pore diffusional limitations may be avoided in the same FT reactor using impeller speed in excess of 600 rpm and average particle size smaller than 425 μm.

ECT-Based Reaction Runs

FTS runs were performed at different temperatures and at the constant pressure of 21 atm using syngas with H$_2$:CO ratio of 2:1. The rise in dispersed (gas) phase hold-up (since the contribution due to the alumina supported catalyst particles has been previously determined to be temperature-insensitive) with temperature seemed to level off at higher temperature as may be seen in Figure 9 hence, the behaviour was described by;

$$\varepsilon_D = \varepsilon_{D_0} + b_0 \left[1 - \exp(-b_1 \theta) \right] \tag{16}$$

where θ is the dimensionless temperature ($\theta = T-T_0/T_0$), with T_0 as the room temperature (=295 K). Nonlinear regression of the data provided, $\varepsilon_{D0} = 0.04\pm0.0013$, $b_0 = 19.54\pm0.047$ and $b_1 = 0.0048\pm0.0002$. The change in gas phase hold-up over the reaction temperature range employed is more than what was expected due to mere gas volume expansion (6% from 493 to 523 K) since ε_G increased by more than 19% over the same temperature range suggesting that extant liquid phase properties as product accumulation continued was probably responsible for the large variation in gas hold-up with temperature. This finding is in line with the original proposition of reaction-induced change in hydrodynamic attributes. Clearly, the sensible change in gas phase hold-up due to product accumulation would also affect mixing characterisitics and thus, reaction rate. Indeed, this increase in gas holdup with temperature was also reported by others (*18*, *19*) due to decreased the liquid viscosity and surface tension. On the other hand, it is evident from Figure 9 that the reaction rate followed the expected Arrhenius behaviour with b_2 estimated as the Arrhenius number, $E/RT_0 = 26.58$, for the FT reaction at T_0 and hence, an activation energy, E, of 65.2 kJ mol^{-1} (cf. Eq. (17)).

$$\left(-r_{rxn} \right) = r_0 \exp \left(-\frac{b_2}{(\theta + 1)} \right) \tag{17}$$
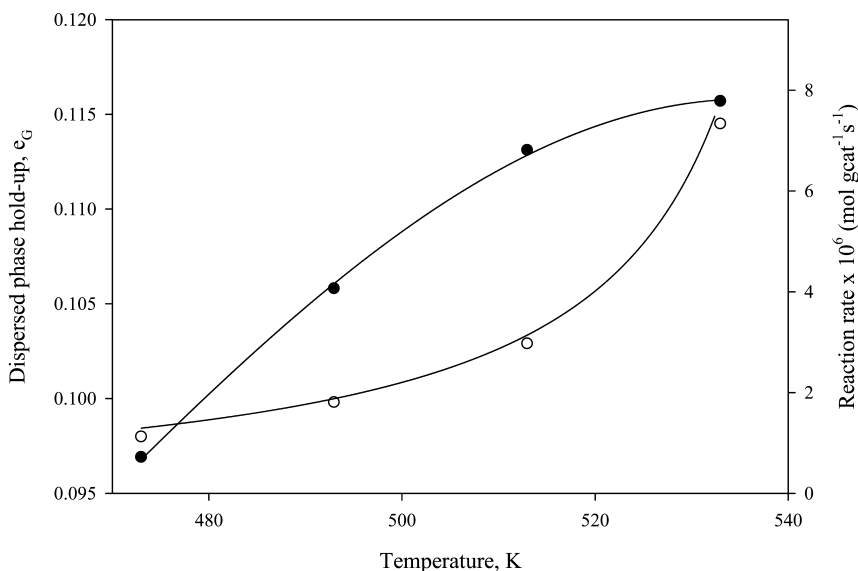

Figure 9. Dispersed phase hold-up (●) and reaction rate (○) as function of temperature.

Thus, combining Eqs. (16) and (17), the coupling between reaction rate and dispersed phase hold-up may be expressed by;

$$\left(-r_{rxn}\right) = r_0 \exp\left[\cfrac{-b_1 b_2}{b_1 - \ln\left\{ \cfrac{b_0 - \left(\varepsilon_D - \varepsilon_{D_0}\right)}{b_0} \right\}} \right] \tag{18}$$

The effect of syngas composition on FTS rate is shown in Figure 10. The profile is strongly skewed towards the high H_2 mole fraction, y_{H2}, due to relatively weak adsorption of H_2 on the catalyst surface in the presence of CO.
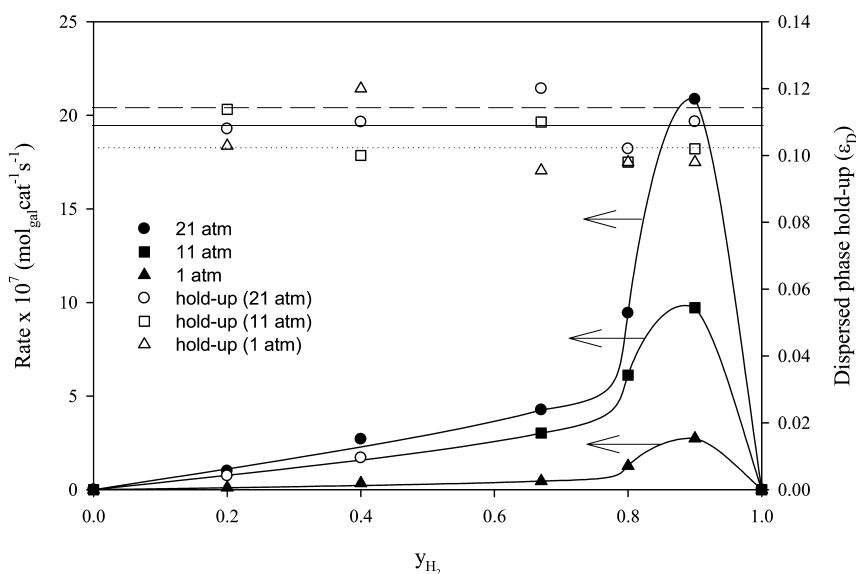

Figure 10. Effect of reaction rate and dispersed hold-up on syngas feed composition at T = 523 K.

The latter is reportedly more strongly chemisorbed on the same site as H_2 (*20*). Interestingly, the associated gas phase hold-up is practically constant over the feed composition, y_{H2}, values used as seen on the same plot regardless of the total pressure. This indicates that the change in liquid phase properties as result of product accumulation was probably similar for different syngas concentrations.

Figure 10 further shows that the reaction rate–composition profiles are similarly shaped at all three total operating pressures investigated. The optimum composition is a feed gas with H_2:CO ratio of 9:1 in all cases. These qualitative features suggest that the FT reaction mechanism was probably unchanged at the different operating pressures used. Indeed, as evident from Figure 11, the hydrocarbon synthesis rate has a linear dependency on the total operating pressure with a proportionality constant of $9.73\pm0.13 \times 10^{-7}$ mol gcat^{-1} s^{-1} atm^{-1}.
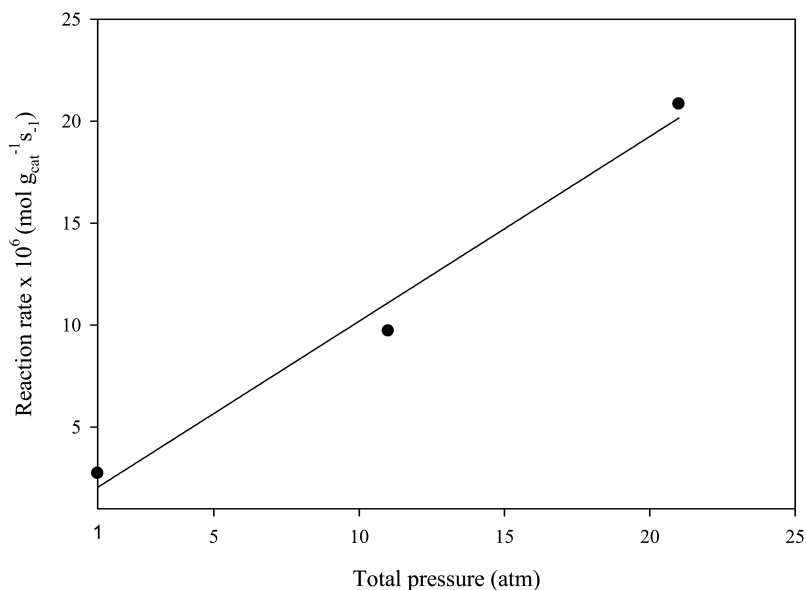

Figure 11. Reaction rate as function of total pressure.

The chain growth probability, α, was obtained from a fit of the individual hydrocarbon formation rate to the Anderson-Schulz-Flory model given by:

$$r_{C_n} = k(1-\alpha)^2 \alpha^{n-1} \tag{19}$$

Figure 12a displays the variation of α with feed compostion at the three operating total pressures used. However, Figure 12b illustrates the trend in olefin-to-paraffin ratio, ROP, for each carbon number with respect to feed composition. The decreasing ROP with increased feed H_2 mole fraction is a reflection of the fact that nearly identical surface H:C ratio is required for the formation of olefins and paraffins as the chain carbon number increased.
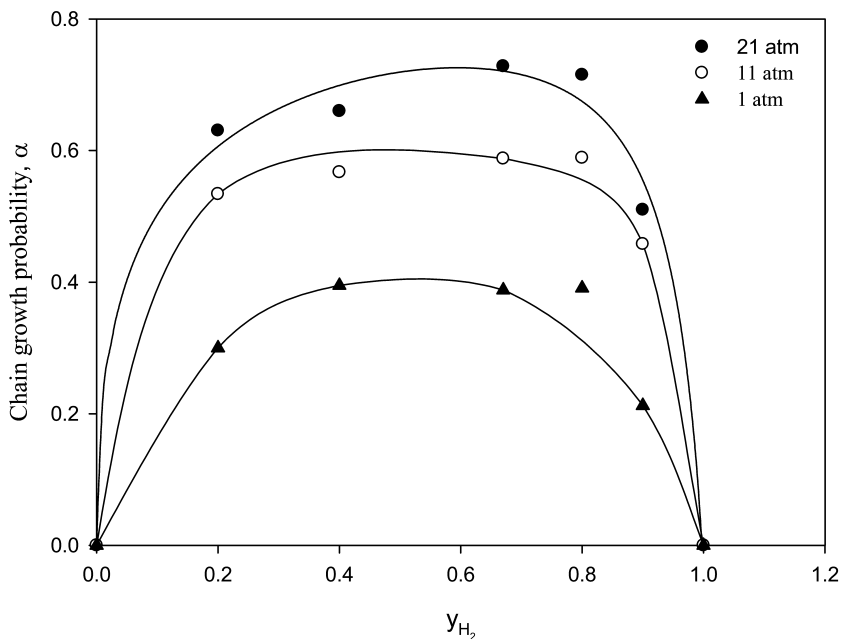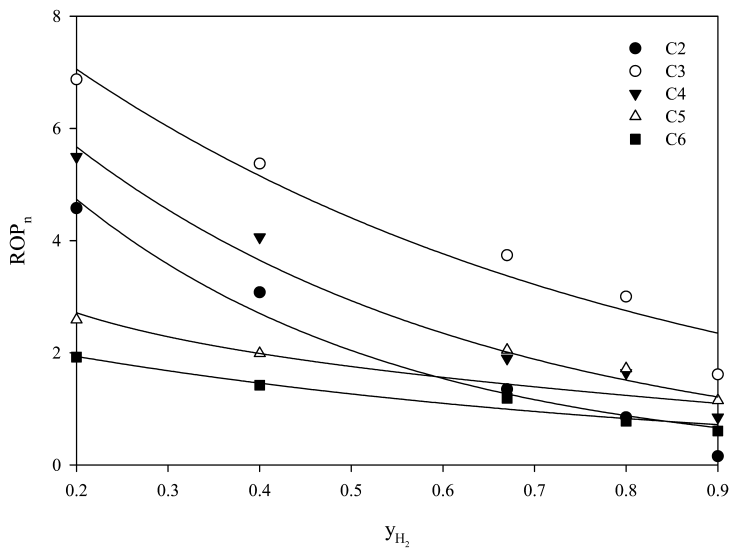
Figure 12a

Figure 12b

*Figure 12. (a) Effect of syngas feed composition on chain growth probability, α.
(b) ROP$_n$ as function of feed composition, y_{H2}.*

In Synthetic Liquids Production and Refining; de Klerk, A., et al.;
ACS Symposium Series; American Chemical Society: Washington, DC, 2011.

As was observed in the case of rate envelopes, the shape similarity of the curves in Figure 12a is indicative of a common reaction mechanism regardless of the pressure employed. In particular, the "plateau" in chain growth probability values for syngas composition with $0.4 \leq y_{H2} \leq 0.8$ implicates the existence of a common surface monomeric species in the propagation step – most likely a CH_2 species - for higher hydrocarbon formation. However, the average carbon chain length, $\bar{n} = \dfrac{1}{1-\alpha}$, clearly increased with total pressure as may be expected for a surface polymerization reaction. In fact, the linear expression (cf. Figure 13);

$$\bar{n} = \bar{n}_0 + \psi P_T \tag{20}$$

governs the relationship between $\bar{n}$ and P_T. where, $\bar{n}_0$ is the average carbon number for FTS at subatmospheric pressure and estimated as 1.48 and ψ is the pressure coefficient for chain growth obtained as 0.087 atm^{-1} for the present catalyst.
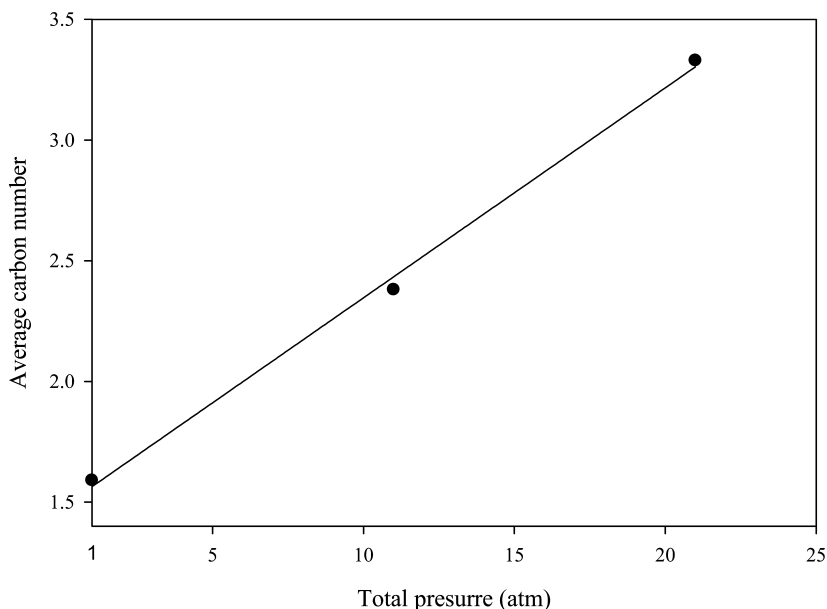

Figure 13. Average carbon number as function of total pressure.

This finding is in agreement with the reports of other investigators (*21, 22*) on the beneficial effects of high pressure operation for FTS although other FT catalysts will be characterized by different values of $\bar{n}_0$ and ψ. Eq. (20) may be used to estimate the required total pressure for a desired value of $\bar{n}$ or α.

The behaviour of the olefin-to-paraffin ratio, ROP as a function of hydrogen mole fraction in the feed, y_{H2}, plotted in Figure 14 reveals that propene and butene are the most favoured olefins on the catalyst since the maximum ROP may be located between carbon number 3 to 4 across the range of syngas compositions studied. The ROP values for C_{7+} species would appear to be well below 2 suggesting that the rate with which the olefins or paraffins for the higher hydrocarbons are produced was probably the same due to the nearly identical H:C ratio in these species at n ≥7. Additionally, the gas phase composition of the species may be less reliable because of their higher solubilities in the liquid phase and the relatively smaller amounts produced under FTS conditions.
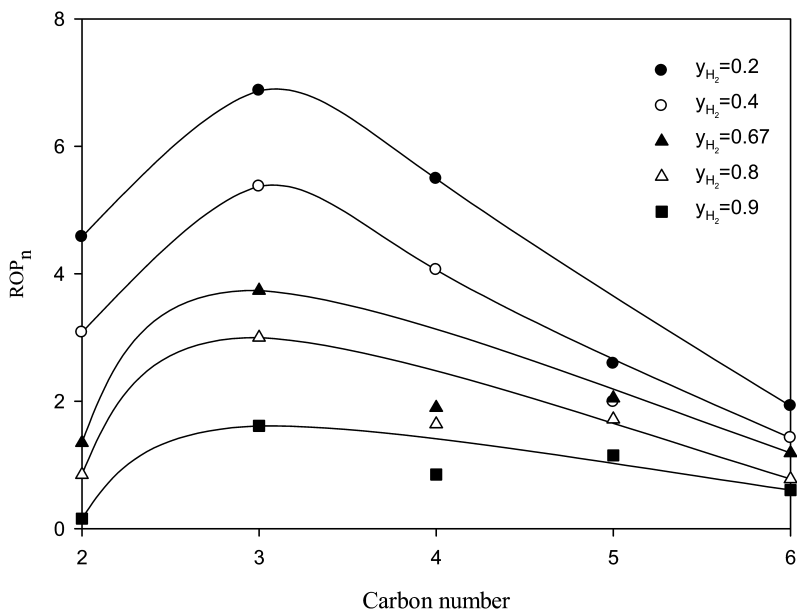

Figure 14. The behaviour of olefin-to-paraffin ratio, ROP as function of syngas feed composition at different carbon number.

The relationship between ROP and the carbon number, n, irrespective of the syngas composition may be adequately described by:

$$ROP = \frac{\Lambda}{\left[1 + \omega \left(n - \eta \right)^2 \right]} \tag{21}$$

where Λ represents the maximum ROP value with and η as the carbon number at which it may be produced while ω is an olefin attenuation index .

Table 2 contains the estimates of these parameters obtained from nonlinear regression of the data.

Table 2. The estimate of parameter of Eq. (21)

Feed composition, $yH2$	Model parameters		
	Λ	η	ω
0.2	6.97±0.04	3.14±0.02	0.40±0.01
0.4	5.42±0.03	3.21±0.02	0.50±0.01
0.67	3.26±0.08	3.28±0.08	0.44±0.01
0.8	3.18±0.16	3.30±0.17	0.58±0.03
0.9	1.25±0.10	3.89±0.30	0.27±0.02

It is manifest from this table that while olefin selectivity (Λ) decreased with increasing feed H_2 content, the carbon chain length corresponding to maximum ROP (η) exhibited an opposing trend. It would therefore seem that it is infeasible to simultaneously optimize both olefin selectivity and carbon chain length by manipulating only feed composition.

Effect of Temperature and Time-on-Stream

The role of temperature and time-on-stream on dispersed phase hold-up is shown in Figure 15. The transient profile has a characteristic sigmoid shape at all temperatures and thus, the thermotemporal behaviour may be expressed as:

$$\varepsilon_D = \varepsilon_{D_0} + \varepsilon_{D_1}\left[1 - \exp\left(-\zeta t\right)\right]^{\upsilon} \tag{22}$$

where $\varepsilon_{D,0}$ is the initial dispersed hold-up, $\varepsilon_{,D1}$ is the deviation between the ultimate dispersed phase hold-up (at infinite time) and the initial value, ζ is the time constant for the dispersed phase and υ is an empirical exponent.

Table 3 displays the estimates from nonlinear regression of the data. It is apparent that all the model parameters (with the exception of υ estimated as 2.0) are temperature-sensitive. In particular, while ε_{D0} reflects essentially the contribution due to thermal expansion of the gas phase, ε_{D1} is indicative of a reaction-induced involvement. Interestingly, an Arrehnius treatment of the data provided an activation energy, E_{D0} of 5.6 kJ mol^{-1} (symptomatic of a physical process and in agreement with the activation energy, i.e 5.8 kJ mol^{-1}, found for the data in Figure 7 under non-reactive conditions) for the initial dispersed phase hold-up, ε_{D0} and a corresponding, but larger, value, E_{D1} of 23 kJ mol^{-1} for ε_{D1} confirming its association with a reaction-controlled step. The empirical exponent represents the number of dispersed phase entities involved in any interaction occasioning a change in the hold-up with time-on-stream. A value of 2.0 for υ suggests that at least 2 gas bubbles are implicated in the bubble-bubble interaction.
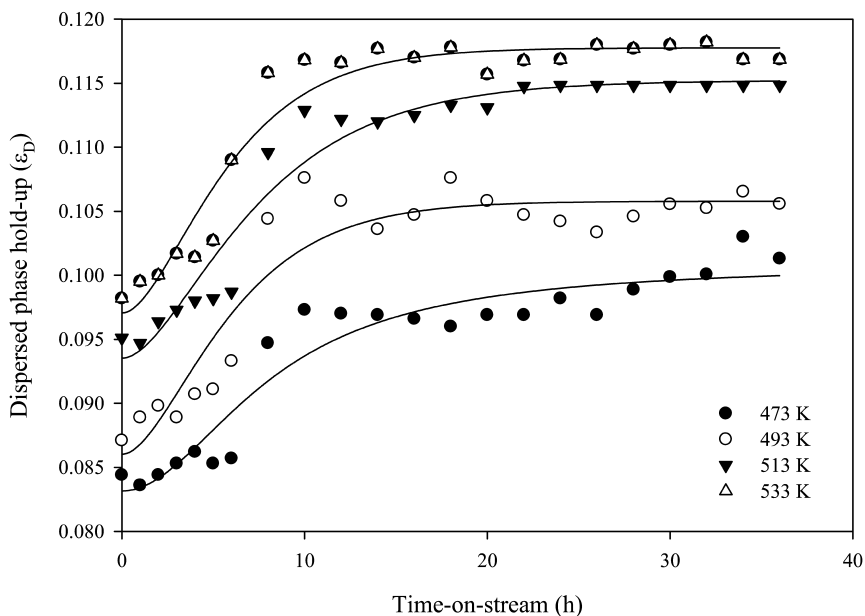
*Figure 15. Dispersed phase hold-up as function of TOS at different temperature.
Reaction conditions: H2:CO =2:1 at total pressure of 21 atm.*

Table 3. Estimates of parameter of Eq. (22)

Temperature	ε_{D0}	ε_{D1}	ζ	υ
473 K	0.0830±0.0021	0.0168±0.0004	0.1566±0.0040	2.0
493 K	0.0860±0.0017	0.0199±0.0004	0.2276±0.0046	2.0
513 K	0.0922±0.0023	0.0222±0.0006	0.2300±0.0058	2.0
533 K	0.0970±0.0030	0.0339±0.0010	0.2333±0.0071	2.0

As may be seen in Figure 16, the effect of total operating pressure on the dispersed phase hold-up with time-on-stream also followed a first-order exponential rise to an ultimate value. Consequently, a model structurally similar to Eq. (16) may be used to represent the behaviour, namely;

$$\varepsilon_{D,P} = \varepsilon_{D_0,P} + \varepsilon_{D_1,P}\left[1 - \exp(-\varsigma_P t)\right] \tag{23}$$

The resulting parameter estimates are provided in Table 4.

Table 4. Values of the model parameter in Eq. (23)

Pressure (atm)	$\varepsilon_{D0,P}$	$\varepsilon_{D1,P}$	ζ_P
1	0.0533±0.0008	0.0682±0.0010	0.1712±0.0026
11	0.0641±0.0013	0.0567±0.0011	0.2129±0.0043
21	0.0673±0.0035	0.0510±0.0026	0.4068±0.0209

Consistent with earlier finding (cf. Figure 8) on the relatively mild influence of pressure (compared to temperature) on gas phase hold-up, the results here reinforce the modest role of operating pressure on gas hold-up during reaction, Even so, there is a discernible trend in the values of the model parameters with increased pressure.
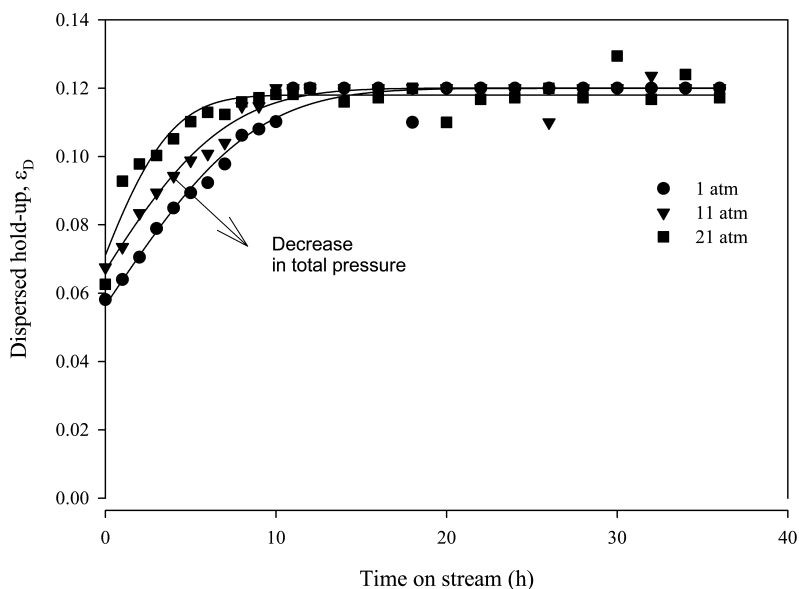

Figure 16. Transient profile of the dispersed phase hold-up at different total pressures, reaction condition: $H_2:CO=9:1$, Temperature = 498 K.

Figure 17 shows that the total hydrocarbon synthesis rate followed a 1st order exponential rise to a final steady-state value with time-on-stream. Although this behaviour is similar to the stirred reactor dynamics under non-reactive conditions (cf. Figure 3), the difference in time-constants is evident when data in Figure 3 and 17 were individually fitted to the expression:

$$y_P = y_P^{SS} \left[1 - \exp(-t/\tau_P) \right] \tag{24}$$

where y_P is the time-dependent response of the operation P to a step-change in y and y_P^{SS} is the final or ultimate value of y at steady-state while τ_P is the time-constant for the particular operation. The data in Figure 3 were collected when the reactor was operated under identical conditions (temperature and pressure to FT reaction) but using pure Ar as the feed before an abrupt switch to pure N_2 stream. Nonlinear regression of the data in both plots to Eq. (24) provided τ_P for the non-reactive conditions as 26 mins while the reaction rate has a corresponding value of 1.28 hours. This clearly suggests that the net reaction relaxation time constant (a hybrid of the surface relaxation time constants for all elementary steps) during FTS is larger than the resistance due to mixing. The data in Figure 3, also showed an initial transport lag of about 6 mins. A mixing time constant of 26 mins confirms that the reaction dynamics (monitored for about 48 hours) was not disguised by fluid phase hydrodynamics or mixing.
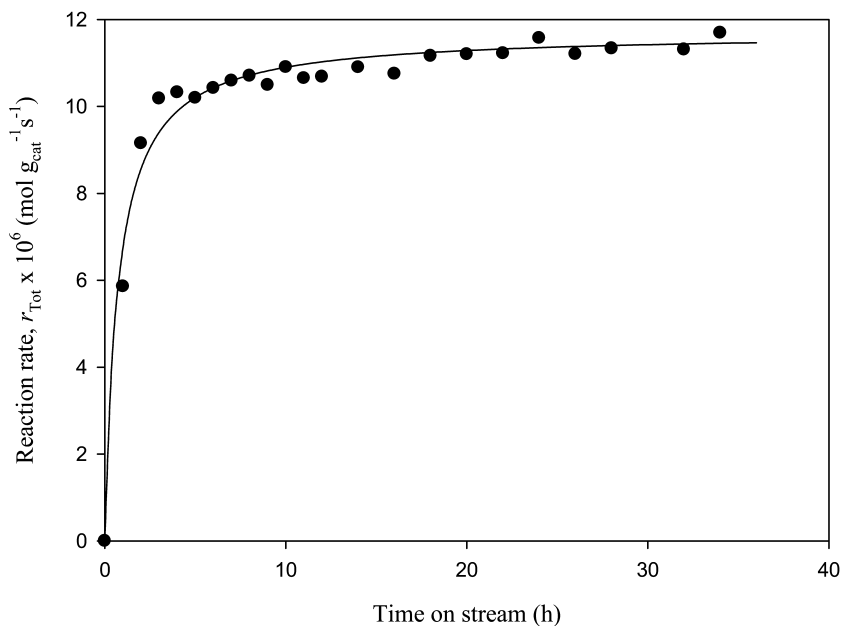

Figure 17. Reaction rate profile with time-on-stream at 498 K, 21 atm using feed with H_2:CO=9:1.

Interestingly, the plots in Figure 18(a, b) reveals that the individual hydrocarbon species also experienced similar reaction dynamics albeit characterized by different formation time-constants (reciprocal of the surface rate velocity) when the production rate data were fitted to Eq. (24). These estimates are summarized in Table 5.
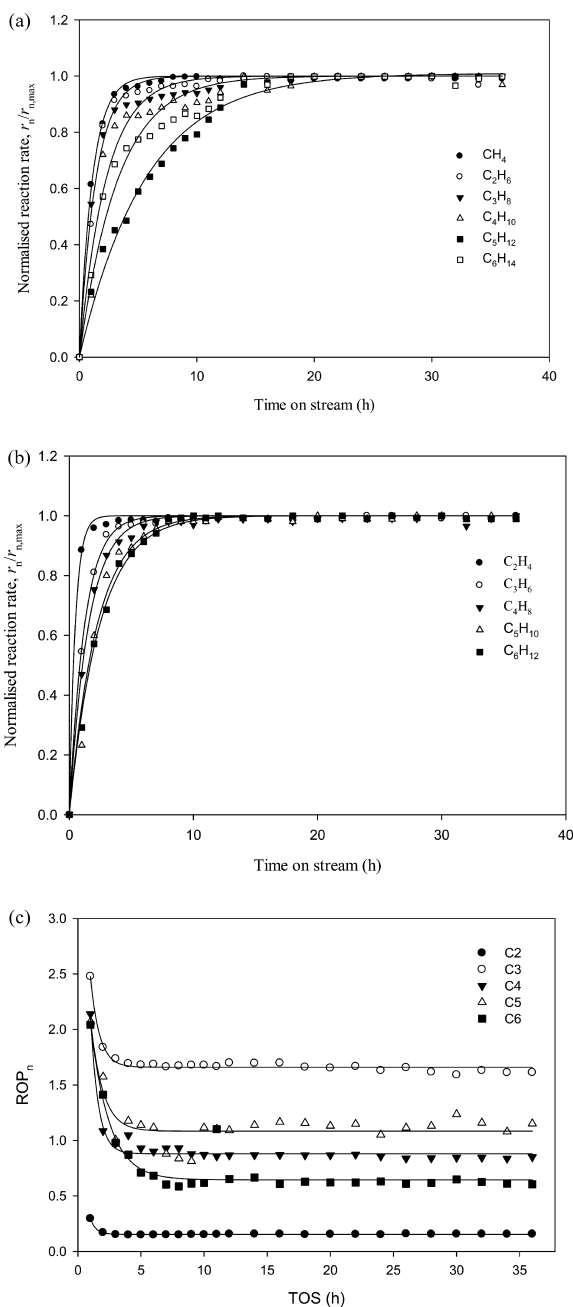
Figure 18. (a) Normalised reaction rate history of individual paraffinic species at T = 498 K, and 21 atm with a feed H_2:CO ratio= 9:1. (b) Normalised reaction rate history of individual olefinic species at T = 498 K, and 21 atm with a feed H_2:CO ratio= 9:1. (c) ROP as a function of time-on-stream, T = 498 K, y_{H2}=0.9.

Table 5. Estimation of time-constant, τP, (hours) for individual hydrocarbons from Eq. (24)

	C_1	C_2	C_3	C_4	C_5	C_6
Paraffins	1.09	1.40	2.27	3.27	4.42	5.64
Olefins	-	0.48	1.22	1.54	2.23	2.43

These estimates revealed that for any carbon number, olefin has a shorter relaxation surface time constant than paraffin indicating that it is more reactive and serves as the precursor to paraffin. Additionally, the relationship between τP and carbon number, n, for both homologous series seemed to be adequately captured by;

$$\tau_P = \phi n^{\xi}$$ (25)

with the pair φ and ξ as 0.91 and 0.95 for paraffins and 0.20 and 1.47 for olefins. The power-law dependency of the relaxation time constant on carbon chain length is consistent with the polymerization nature of the FT reaction. Figure 18c suggests that the ROP value initiallydropped with time-on-stream but reached an essentially constant value after about 10 hours for all hydrocarbon species. Even so, it is apparent that the time to complete this initial drop increased with carbon number.

The associated chain growth probability with time-on-stream is also shown in Figure 19, The data suggests an initial regime (within the first 5 hours –Region I) where the chain growth factor increased linearly with TOS followed by a longer period of about 25 hours (Region II) during which α was essentially constant and a final stage (Region III) where another linear increase with TOS was experienced. However, the chain growth factor was somewhat insensitive to temperature.This behaviour has also been observed in previous studies (*2, 13, 20*), In particular, the relation between α and temperature, T may be written as;

$$\alpha = \frac{r_p}{r_p + r_t} = \frac{A_p f_p \exp(-E_p / RT)}{A_p f_p \exp(-E_p / RT) + A_t f_t \exp(-E_t / RT)}$$

$$= \frac{1}{\left[1 + \dfrac{A_t f_t}{A_p f_p} \exp\{-(E_t - E_p) / RT\}\right]}$$ (26)

where both A_p and A_t are the propagation and termination rate frequency factors respectively with f_p and f_t as associated functions of feed composition i.e. H_2 and CO partial pressures for the propagation and termination steps respectively. It is apparent that for a given composition, the variation of α with increasing temperature may either show a decreasing ($E_t > E_p$) or increasing ($E_t < E_p$) trend or be somewhat insensitive or even diffused depending on the relative magnitude of

E_p and E_t and the ratio $A_t f_t/A_p f_p$ This explains why different effects of temperature has been reported in the literature (*22*).

The changes observed in the present work implicate an ongoing interaction between the physicochemical properties of the reaction medium and reaction metrics and hence, the transient behaviour observed in the dispersed phase hold-up as reaction progressed. While the initial rise in α value in Region I is a reflection of the intrinsic propagation step in hydrocarbon synthesis on the catalyst surface, the plateau in Region II suggests an equilibration between the liquid phase and the gas phase individual hydrocarbon composition. These two regimes parallel the behaviour seen in the dispersed phase hold-up with time-on-stream. The trend seen in Region III may, however, be due to the production of hydrocarbons from the break-down of waxy deposit (which had accumulated in the previous two regions). Although gas phase CO conversion would remain constant in this regime, hydrocarbon production would be a combination of the intrinsic FT propagation step as well as the cracking of waxy deposit on the catalyst surface and hence, a rejuvenative increase in α-value. Intuitively, Region III itself would attain a new climax and then level off, although the 2-day run period was probably insufficient to realize this proposed stage. The dispersed phase hold-up would not be affected in Region III since the same hydrocarbon species were produced but only in greater amounts and hence, no discernible variation in the physicochemical properties of the liquid phase composition.
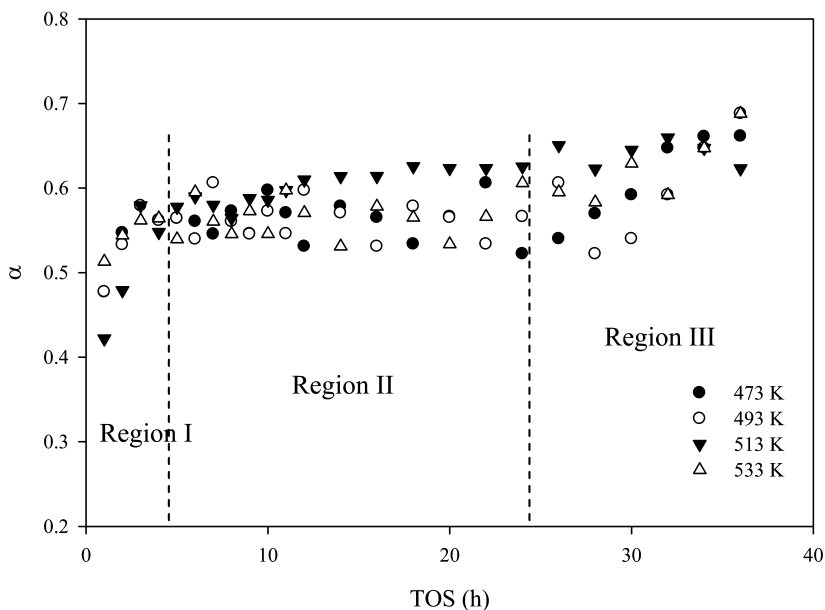

Figure 19. ASF chain growth factor as function of time-on-stream (TOS), P = 21 atm.

Figure 20 indeed confirms that CO conversion also rose to a final steady-state value consistent with the individual hydrocarbon production history.
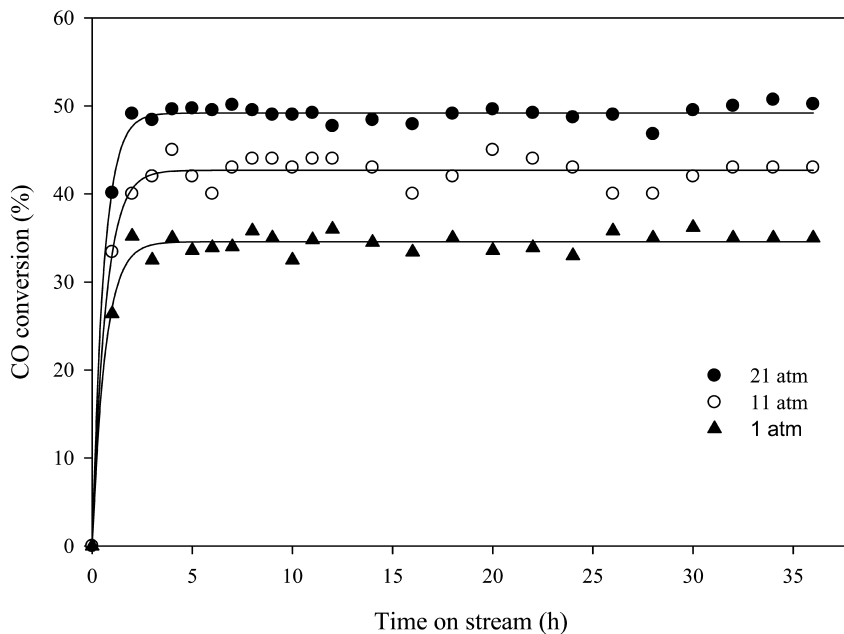

Figure 20. CO conversion history for FTS at T =: 498 K, and syngas ratio H_2:CO=9:1.

Conclusions

The non-invasive monitoring of an FTS slurry reactor using electrical capacitance tomography has shown that the multiphase hydrodynamic attributes such as dispersed phase hold-up (and by inference solid recirculation rate and distribution) are intimately intertwined with the reaction metrics (rate, product selectivity, etc). This coupling is due to the changing physicochemical properties of the liquid phase medium as product accumulation continues in the course of the reaction. This phenomenon is especially important in FTS operation since it can help to unlock some of the peculiar reaction performance (evolution of chain growth factor, α) observed over a long run time and we have attermpted to understand this association using ECT probing in the present work. This dynamic feedback between transport and reaction processes has not been previously unabmiguously identified. However, the present analysis has provided, for the first time, a quantitative relation between reaction rate and dispersed phase hold-up. Furthermore, the data demonstrated that under non-isothermal conditions, changes in gas phase hold-up could not be accounted for by simple thermal expansion. Indeed, the sigmoid-shaped thermotemporal relationship for the disepred phase hold-up in the slurry FT reactor was also derived and shown

to be a combination of volumetric expansion and a reaction-controlled increment. Although the gas phase hold-up increased linearly with operating total pressure, the accompanying improvement was relatively small compared to thermal or reaction-induced effects. Analysis of the FT reaction rate data showed that the olefin-to-paraffin ratio, ROP, is has a maximum at carbon number between 3 and 4. Moreover, ROP is also a strong function of the hydrogen composition in the feed mixture and this was confirmed by the dependency of the parameters of the proposed ROP model on feed H_2:CO ratio.

The approach taken in this study (tomographical analysis and empirical modeling) represents a new paradigm in the treatment of reaction rate data from a gas-solid-liquid reactor and over time, would help elucidate some of the apparent anomalous or pathglogical behaviour observed in slurry reactor systems. The ECT-based models developed may also be reliably employed for process simulation and optimization as well as providing additional insights into the fundamental nature of the reaction chemistry (since the tomographical inquiry is non-obtrusive)

Acknowledgments

References

1. Bai, L.; Xiang, H.-W.; Li, Y.-W.; Han, Y.-Z.; Zhong, B. *Fuel* **2002**, *81*, 1577–1581.
2. Bukur, D. B.; Sivaraj, C. *Appl.Catal., A* **2002**, *231*, 201–214.
3. Adesina, A. A. *Appl.Catal., A* **1996**, *138*, 345–367.
4. Joshi, J. B. *Chem. Eng. Commun.* **1980**, *5*, 109.
5. Joshi, J. B.; Sharma, M. M. *Can. J. Chem. Eng.* **1977**, *65*, 683.
6. Forrester, S. F.; Reilly, C. D.; Carpenter, K. J. *Chem. Eng. Sci.* **1998**, *53*, 603–615.
7. Sawant, S. B.; Joshi, J. B. *Chem. Eng. J.* **1979**, *18*, 87–91.
8. Murthy, B. N.; Kasundra, R. B.; Joshi, J. B. *Chem. Eng. J.* **2008**, *141*, 332–345.
9. Hardiman, K. M.; Cooper, C. G.; Adesina, A. A. *Ind. Eng. Chem. Res.* **2004**, *43*, 6006–6013.
10. Cheng, C. K.; Foo, S. Y.; Adesina, A. A. *Catal. Today*, *164* (1), 268–274.
11. Chu, W.; Chernavskii, P. A.; Gengembre, L.; Pankina, G. A.; Fongarland, P.; Khodakov, A. Y. *J. Catal.* **2007**, *252* (2), 215–230.
12. Jacobs, G.; Chaney, J. A.; Patterson, P. M.; Das, T. K.; Davis, B. H. *Appl. Catal., A* **2004**, *264* (2), 203–212.
13. Cooper, C. G.; Nguyen, T.-H.; Lee, Y.-J.; Hardiman, K. M.; Safinski, T.; Lucien, F. P.; Adesina, A. A. *Catal. Today* **2008**, *131* (1-4), 255–261.

14. Yaluris, G.; Larson, R. B.; Kobe, J. M.; González, M. R.; Fogash, K. B.; Dumesic, J. A. *J. Catal.* **1996**, *158*, 336–342.
15. Mekhemer, G. A. H.; Abd-Allah, H. M. M.; Mansour, S. A. A. *Colloids Surf., A* **1999**, *160* (3), 251–259.
16. Morterram, C.; Colluccia, S.; Chionino, A.; Bocuzzi, F. *J. Catal.* **1978**, *54*, 348.
17. Vilar, G.; Williams, R. A.; Wang, M.; Tweedie, R. *J. Chem. Eng. J.* **2008**, *141*, 58–66.
18. Bell, A. T. *Catal. Rev. − Sci. Eng.* **1981**, *23*, 203–232.
19. Ma, W.; Ding, Y.; Carreto-Vaquez, V. H.; Bukur, D. B. *Appl. Catal., A* **2004**, *268*, 99–106.
20. Satterfield, C. N.; Huff, G. A. *Chem. Eng. Sci.* **1980**, *35*, 195–202.
21. Neathery, J. K.; Davis, B. H. *Catal. Today* **2003**, *84*, 3–8.
22. Vo, D. V. N.; Adesina, A. A. *Appl. Catal., A* **2011**, in press.